Received: 3 May 2020 | Revised: 19 February 2021 | Accepted: 22 February 2021
DOI: 10.1002/esp.5110

RESEARCH ARTICLE

ESPL WILEY

The variability of antidune morphodynamics on steep slopes

Ivan Pascal[1] | **Christophe Ancey**[1] | **Patricio Bohorquez**[2]

[1]Laboratoire Hydraulique Environnementale, École Polytechnique Fédérale de Lausanne, Lausanne, 1015, Switzerland

[2]Centro de Estudios Avanzados en Ciencias de la Tierra, Universidad de Jaén, Campus de las Lagunillas, Jaén, 23071, Spain

Correspondence
Ivan Pascal, Laboratoire Hydraulique Environnementale, École Polytechnique Fédérale de Lausanne, 1015 Lausanne, Switzerland.
Email: ivan.pascal@epfl.ch

Funding information
Ministerio de Ciencia e Innovación de España, Grant/Award Number: CGL2015-70736-R

Abstract

Steep streams on rough beds are generally characterised by supercritical flow conditions under which antidunes can develop and migrate over time. In this paper, we present flume experiments that we conducted to investigate the variability of antidune geometry and migration celerity, a variability observed even under steady-state conditions. Quantifying this variability is important for river morphodynamics, hydraulics and paleohydraulics. We imposed moderate to intense bedload transport rates at the flume inlet to assess their effects on antidune morphodynamics for near-constant values of the mean bed slope. The bed elevation profile was monitored for each experiment with high spatial and temporal resolution. Upstream migrating antidunes were observed along most of the flume length. Considering single values for wavelength and celerity was not sufficient to describe the antidune behaviour in these experiments. By using spectral analysis, we identified the variability ranges of bedform shape and celerity. Interestingly, migration celerity increased with increasing antidune wavelength; the opposite trend was reported for dunes in other studies. Antidunes were more uniform and migrated faster for higher sediment feeding rates. Scaling the spectra made it possible to find a general dimensionless relationship between antidune wavelength and celerity. This framework provides a novel method for estimating the mean bedload transport rate in the presence of upstream migrating antidunes.

KEYWORDS
antidune, bedform variability, bedload transport, flume experiments, paleohydraulics, river morphodynamics

1 | INTRODUCTION

In nature, riverbeds usually exhibit bedforms of various spatial and temporal scales, which can migrate over time. The occurrence of a given bed morphology depends on the hydrodynamical and sedimentary conditions (sediment properties, supply, etc.). Studying bedform dynamics is important to understand both the evolution of alluvial environments and the implications for flow resistance and sediment fluxes. Antidunes are bedforms typical of supercritical (or near critical) flows on steep slopes and can be observed also for upper-flow regimes on mild slopes. The term 'antidune' was originally proposed by Gilbert and Murphy (1914) to identify two-dimensional bedforms that migrate upstream, contrary to dunes. Nowadays, antidunes are defined as sinusoidal shaped bedforms for which the water surface is in phase with the bed undulations, according to Kennedy (1961). This definition is adopted in the present paper. Antidunes are associated with step-pool morphologies (Chin, 1999; Grant, 1994; Whittaker & Jaeggi, 1982) and may co-exist with cyclic steps in transcritical flows (Alexander, 2008; Cartigny et al., 2014; Slootman & Cartigny, 2020). Since the pioneering work by Kennedy (1961, 1963, 1969), great efforts have been dedicated to studying antidunes formation and their stability domains (e.g. Andreotti et al., 2012; Bohorquez et al., 2019; Bose & Dey, 2009; Carling & Shvidchenko, 2002; Coleman & Fenton, 2000; Colombini, 2004; Colombini & Stocchino, 2005, 2008, 2012; Deigaard, 2006; Di Cristo et al., 2006; Engelund, 1970; Greco et al., 2018; Hayashi, 1970; Huang &

Chiang, 2001; Kubo & Yokokawa, 2001; Parker, 1975; Reynolds, 1965; Vesipa et al., 2012). In parallel, experimental studies on antidunes have been performed to test theoretical and numerical frameworks and to investigate the main physical mechanisms governing these bed instabilities (e.g. Cao, 1985; Guy et al., 1966; Mettra, 2014; Recking et al., 2009). In paleohydraulic studies, antidunes receive special attention because they are important proxies of hydraulic and sedimentary conditions (e.g. Carling et al., 2009; Shaw & Kellerhals, 1977). Also, downstream migrating antidunes were early documented in experiments (e.g. Kennedy, 1961), but a criterion for antidune migration direction has been formalised only recently (Núñez-González & Martín-Vide, 2011). Experimental studies have mostly focused on downstream migrating bedforms (dunes and bars) rather than on antidunes. This likely reflects the high demand of methods to quantify dune geometry and contribution to the sediment fluxes for streams on gentle slopes. To the best of our knowledge, Simons et al. (1965) can be credited with the first framework for computing the contribution of downstream migrating dunes to the mean bedload discharge. The existence of bedload transport pulses has been related to bedform migration (Gomez et al., 1989), a relationship that has been investigated in gravel-bed flumes through experimental investigations into alternate bars (e.g. Dhont & Ancey, 2018; Palucis et al., 2018). When alternate bars are associated with near-critical flows, antidunes may develop locally and contribute to sediment transport (see Movie S3 in Dhont & Ancey, 2018).

For steep slopes, Recking et al. (2009) considered data regarding antidunes occurrence and proposed new specific relationships for predicting the dominant wave geometry. Migrating antidunes of variable wavelength have been observed in gravel-bed rivers (see Video Clip S2 in Froude et al., 2017). In his flume experiments on steep slopes, Mettra (2014) observed antidunes characterised by varying shapes and migration celerities and investigated the contribution of upstream migrating antidunes to the bedload flux. Based on the model proposed by Simons et al. (1965), he proposed two expressions for estimating the mean and maximum local bedload transport rates (involving mean and maximum values of antidune amplitude and celerity). Ancey and Pascal (2020) monitored bedload transport in a narrow flume in the presence of upstream migrating antidunes and reported bedload pulses whose period was consistent with the antidune migration period. As far as we know, an integral relationship for computing the sediment flux associated with upstream migrating antidunes is not yet available. This expression should also include the potential scale dependencies between wave geometry and migration celerity. Upstream migrating antidunes travel in the opposite direction of the bedload flux which cannot be decomposed straightforwardly in a fraction that contributes to the migration of a given antidune and in a passive fraction. This peculiarity prevents the direct application of the integration frameworks already defined for downstream migrating dunes by Nikora (1984) and Guala et al. (2014).

Running well-controlled flume experiments provides useful insights into the bedform dynamics under steady-state conditions. We performed experiments in a steep flume in which we monitored the bed topography with high spatial and temporal resolution. We used spectral analysis to quantify the variability of antidune geometry and celerity. We analysed how sediment transport rates depended on antidune migration celerity, and how antidune variability, in turn, affected bedload transport. We present the outcomes of this analysis with an emphasis given to antidune wavelength and migration celerity. We provide tentative answers to the two following questions: (i) Does the variability of antidune geometry and migration celerity follow a general trend? (ii) Is it possible to define a method for estimating the mean bedload transport rate associated with upstream migrating antidunes on steep slopes? The findings are discussed, and their potential implications for river morphodynamics, steep-stream hydraulics and paleohydraulics are outlined.

2 | METHODS

2.1 | Experimental arrangement

To investigate antidune morphodynamics, we carried out experiments in a 2.5–m-long 4-cm-wide flume with transparent sidewalls. We used natural gravel with median particle diameter d_{50} = 2.9 mm (d_{16} = 2.5 mm, d_{84} = 3.3 mm) and sediment density ρ_s = 2550 kg m^{-3}. The bed layer thickness was 4 cm on average. We chose well-sorted natural gravel to avoid grain sorting. This choice also had the advantage of simplifying the protocol of bedload transport rate measurement. The flume (Figure 1) was equipped with a sediment feeder, whose supply rate was controlled by a hopper and a rotating wheel. A high-speed camera was mounted over the flume outlet to monitor the sediment discharge. Another camera was used to film bed evolution from the

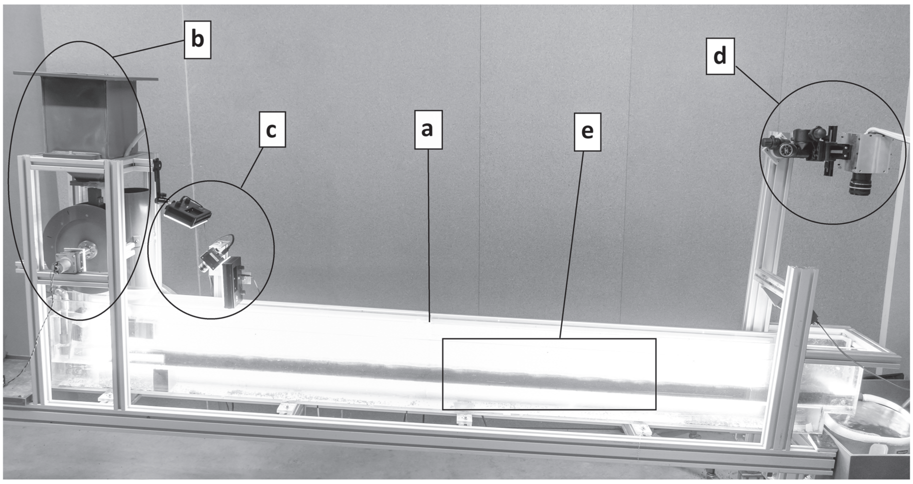

FIGURE 1 Experimental setup: (a) transparent tilting flume for quasi 2D flow, (b) sediment feeding system, (c) camera for monitoring sediment supply at the inlet, (d) camera for monitoring bedload discharge at the outlet, (e) window captured by the side camera (length L_w = 0.75 m)

side. We set the flume width at 4 cm to ensure a reasonable trade-off between ease of data acquisition and representativeness of flow and morphodynamic conditions (relative to those observed in real-world scenarios). This configuration enables the accurate assessment of the quasi-equilibrium state before starting topography data collection and after the run. This condition is fundamental to guarantee that the time series of the bed topography is not significantly influenced by processes related to bed disequilibrium at the flume scale. On the other hand, running experiments in small flumes requires particular attention and accurate systems to control and assess sediment and water supply (see the last part of the next section for details). As the flow conditions and associated bedforms (antidunes in our case) were nearly two-dimensional, we could use simple imaging techniques for extracting bed topography data from side images. The d_{50}/W ratio was kept under 0.1 to mitigate lateral confinement effects.

2.2 | Experimental conditions

The experiments were carried out under steady-state conditions in terms of both water discharge and sediment supply. We ran four experiments with different transport intensities and similar values of mean slope angle, $\overline{\psi}\approx 3^\circ$ (Table 1).

For each run, we imposed a constant sediment feed rate and set the flow discharge per unit width q_w, which ensured balance between erosion and deposition at the flume scale. The sediment feed rates $q_{s,in}$ corresponded to different values of the ratio Θ/Θ_c, where Θ is the Shields number and Θ_c is the critical Shields number (Table 2). We estimated Θ using the relationship

$$\Theta=\frac{g\rho R_b\tan\overline{\psi}}{g(\rho_s-\rho)d_{50}}=\frac{R_b}{d_{50}}\frac{\tan\overline{\psi}}{s-1}, \tag{1}$$

where g is the gravitational acceleration, ρ is the water density, $s=\rho_s/\rho$ is the sediment-to-water density ratio and R_b is the bed hydraulic radius calculated using the Einstein–Johnson sidewall correction method.

The Einstein–Johnson method (Einstein, 1942; Johnson, 1942) is based on the division of the real flow cross-section ($h_0\times W$) in one area A_{sw} dominated by the sidewall friction and one area A_b dominated by the bed friction. Two virtual parallel flumes (flow surfaces equal to A_{sw} and A_b, and rough interface lengths of $2h_0$ and W, respectively) with the same mean flow velocity U and mean energy slope ($\approx\overline{\psi}$) are then considered to compute the hydraulic radii R_{sw} and R_b. This method has proven to give a good approximation of the hydraulic features in supercritical flows in experimental flumes, also compared with more refined methods (Guo, 2015).

The hydraulic radius associated with sidewall friction R_{sw} was calculated by numerically iterating Equation (2) and Equation (3).

$$\frac{\tau_{sw}}{\rho}=\frac{f_{sw}}{8}U^2=gR_{sw}\overline{\psi}. \tag{2}$$

Equation (2) is a Darcy–Weisbach-type law for the flow shearing the sidewalls, where τ_{sw} is the sidewall-related shear stress and f_{sw} is the wall friction coefficient. The latter was determined by the von-Kármán–Prandtl law as

$$(f_{sw})^{-1/2}=2\log\left[Re_{sw}(f_{sw})^{1/2}\right]-0.8, \tag{3}$$

where $Re_{sw}=(4UR_{sw})/\nu$ is the sidewall-related Reynolds number and ν is the kinematic viscosity of the fluid phase.

We then computed the corresponding R_b value, according to its geometrical relationship with R_{sw}, as

$$R_b=\frac{A_b}{W}=h_0\left(1-\frac{2R_{sw}}{W}\right). \tag{4}$$

We estimated the reference flow depth h_0 for the application of the Einstein–Johnson method (note that the mean flow velocity was calculated as $U=q_w/h_0$) using the following Colebrook-type formula for rough fully turbulent flows:

$$(f)^{-1/2}=-2\log\left(\frac{d_{50}}{3.71h_0}\right). \tag{5}$$

We decided to use a friction law to indirectly compute the reference values of h_0 because determining a single representative h value in these very shallow flows requires an insidious arbitrary definition of the bed and water surfaces. The estimated h_0 values showed good consistency with the flow depth h ranges measured for each experiment using image analysis (Table 1). Notably, the reference h_0 value for each experiment was very close to the flow depth double-averaged over the control window and the entire run duration (maximum difference observed for E1, with $\langle\overline{h}\rangle$ = 8.1 mm and h_0 = 8.3 mm).

Table 2 reports the critical Shields values Θ_c estimated from the following equation proposed by Recking et al. (2008):

$$\Theta_c=0.15(\tan\overline{\psi})^{0.275}. \tag{6}$$

Flow conditions were supercritical (Table 2) and turbulent (Re = 3100–4800) for the experiments presented here. Flows were shallow, with a relative roughness d_{50}/h in the 0.3–0.4 range.

TABLE 1 Main parameters for the experimental runs E1–E4

Run	Dur. [min]	$\overline{\psi}$ [°]	$q_{s,in}$ [m^2 s^{-1}]	q_w [m^2 s^{-1}]	$h_0\simeq\langle\overline{h}\rangle$ [m]	h (range) [mm]
E1	77	2.9	$2.0\cdot10^{-5}$	$3.1\cdot10^{-3}$	0.0083	6.5–9.5
E2	37	3.0	$3.5\cdot10^{-5}$	$3.8\cdot10^{-3}$	0.0092	7.5–10.7
E3	36	3.1	$4.8\cdot10^{-5}$	$4.2\cdot10^{-3}$	0.0095	8.0–11.0
E4	47	3.0	$6.1\cdot10^{-5}$	$4.8\cdot10^{-3}$	0.0104	8.5–12.0

TABLE 2 Summary of mean flow velocity, bed hydraulic radius, Shields numbers and Froude number for the experimental runs E1–E4

Run	$U = q_w/h_0$ [m s^{-1}]	R_b [m]	Θ [-]	Θ_c [-]	Θ/Θ_c [-]	$Fr = U/(gh_0)^{1/2}$ [-]
E1	0.37	0.0074	0.085	0.066	1.28	1.31
E2	0.41	0.0083	0.095	0.067	1.43	1.38
E3	0.44	0.0086	0.105	0.068	1.55	1.44
E4	0.46	0.0093	0.108	0.067	1.62	1.45

2.2.1 | Sediment and water supply: Control and monitoring

Since this study focused on the interplay between antidune dynamics and sediment transport conditions, particular attention was dedicated to the systems (i.e. methods and devices) used to control the sediment feeding rate and the water flow rate, and assess their stability in time.

The main components of the sediment feeder (Figure 1) were a sediment tank, a hopper and a motorised wheel. The grains contained in the sediment tank sank through the hopper aperture and were deposited over the wheel surface, which was covered by sandpaper. Subsequently, they were driven to falling by the wheel rotation and the coupled action of a rubber scraper, which prevented periodical avalanches. The hopper aperture was maintained constant for this experimental campaign, whereas the sediment feeding rate was adjusted by selecting the wheel angular velocity. The wheel electric motor (Nidec-Servo DMN37B6HPA motor with 6DG900 gearbox) was chosen during preliminary tests to ensure the desired sediment supply rates. The motor had a torque sufficient to unjam particles stuck between the hopper gate and the wheel. Unjamming was reinforced by adding a 5-mm-thick layer of soft foam between the cylindrical wheel and the sandpaper cover. Particular attention was given to ensuring a minimum filling level of the sediment tank (i.e. a minimum confining pressure) during each run to avoid irregularities in the granular flux inside the hopper. During their fall and before entering the water flow, the sediments were forced to pass over an inclined white plate (illuminated by two LED spotlights) where they were filmed by a Basler acA2000-165um camera (operated at a frame rate of 100 frames per second). The videos collected during the calibration tests allowed us to compute the sediment feeding rates by using the same method presented in this paper for the bedload transport rate monitoring at the flume outlet. The feeding rate series were compared with the sediment samples collected for different sampling durations. These tests made it possible to assess the feeder performances and identify a possible source of fluctuations in the sediment supply: the periodical grain avalanche release over the rotating wheel. This issue was fixed by installing the rubber scraper. The maximum single file size possible with this inlet monitoring setup was sufficient to collect images only for an interval of 750 s; thus, continuous monitoring of the sediment feeding during the experiments was impossible. Others possible sources of fluctuations with this sediment supply system were the misalignment of the wheel axle and the irregularities in the wheel cylindrical shape – especially in the foam coating. Therefore, these sources were carefully inspected before and after each experiment. Moreover, the sediment supply rate steadiness was assessed before and after each run by collecting dry sediment samples at the sediment feeder during 120–180 s.

The water recirculation was controlled with a Pedrollo CP 132A pump. The flow rate was monitored using an Endress+Hauser Proline Promag 50D (DN25) electromagnetic flow-meter mounted on the delivery line (flow velocity measure range 0.01–10 m s^{-1}). The flow-meter relative uncertainty on Q_w was lower than 1.5 % for a total flow rate $Q_w \geq 1.3 \cdot 10^{-4}$ m^3 s^{-1} (that is, the Q_w value for E1). The flow discharge values of the runs were lower than the nominal specifications of the recirculating pump. The flow rate was stabilised by ensuring a sufficient pressure head on the pump delivery line with a valve mounted on the piping. During the experimental runs, we also maintained a constant pressure head on the pump suction line by keeping stable the water level in the outlet reservoir. The water discharge varied smoothly (with a period lower than 5 s) around its mean value (to within 3 %). The water discharge per unit width q_w in the surface flow layer was estimated by subtracting the hyporheic flow discharge from Q_w. The q_w values reported in Table 1 refer to these estimates. We measured the hyporheic flow discharge before and after each experiment by collecting manual samples at the flume outlet.

2.2.2 | Boundary conditions: Specific settings

Specific arrangements were used to set the inlet and outlet boundary conditions. The granular bed was bounded by a vertical perforated plate at the flume outlet. Similarly, a 15-cm-long plastic septum with perforated vertical walls was installed at the upstream bed boundary. Its upper face was covered by artificial roughness elements (transversal rectangular ridges $4 \times 40 \times 2$ mm, streamwise spacing of 4 mm), whose purpose was to limit the flow velocity and thus to avoid triggering an artificial hydraulic jump at the flume inlet. The sediments were fed over this rough fixed surface to mitigate the sediment bursts that would have been caused by the impact of the grains over a fully mobile bed. This arrangement allowed the onset of the hyporheic flow inside the bed layer without sharp vertical deviations of the streamlines over the full bed layer. A honeycomb grid was installed upstream of both the septum and the sediment entrance to stabilise the flow free surface and mitigate the propagation of waves caused by the water inflow.

2.3 | Data collection and image processing for bed topography detection

We monitored the bed topography by filming a 75-cm-long section of the flume from the side. The acquisition window was set at mid-length of the flume, with the upstream side located at $x = 1$ m from the flume inlet ($x = 0$ m). This central position reduced the possible influence of the boundary conditions on antidune dynamics. We collected the images of the bed profile using a Basler A504k camera (operated at a frame rate of 60 or 100 frames per second) equipped with an E Nikon lens (focal length $f = 28$ mm, aperture in the 1–2.8 range). We processed the images (size 1280×200 pixels, resolution 1 px = 0.6 mm) by applying a binarisation filter with a threshold level adjusted to detect the bed–water interface. We then applied a moving average filter (horizontal window of 5 px = 3 mm $\simeq d_{50}$) to smooth small perturbations in the resulting topography caused by particles moving in the bed vicinity. The bed profile sequences were characterised by a temporal resolution of 1 s. The raw images were slightly affected by lens distortion; we decided not to correct it because the opposite effect of perspective distortion of the bed profile was intrinsic to the setup and irreparable in the present context. Therefore, the wavelength measurement accuracy on the bed profiles exceeded the camera nominal resolution and was of the order of d_{50}. To assess wavelength accuracy, we filmed with a lateral view two thin vertical lines drawn on the opposite inner sides of each flume wall at the same cross-section (near the edge of the control window where the distortion effects are maximal), and we measured the virtual distance between these lines on the image. The maximum wavelength error estimate was approximately 2.5 d_{50}.

2.4 | Bedload transport monitoring at the flume outlet

We started to collect bed topography data after the system reached quasi-equilibrium between the sediment supply and the sediment discharge. To check this operational requirement, we monitored the sediment flux at the flume outlet using a basket sampler (with a sampling time in the 60–120-s range). In addition, we filmed the particles transported by the flow over a white board placed at the flume outlet. For this monitoring system, we used the same models of camera and lens as those used for monitoring the bed topography. The 0.055×0.040 m control window was covered by a 190×126 pixel frame. The frame rate was set at 60 or 100 frames per second. To estimate the bedload transport rates at the flume outlet, we used a definition based on particle activity, that is, the number of moving particles per streambed area (e.g. Furbish et al., 2012). Assuming that the mean grain velocity in the control window was constant for a given water discharge, we expressed the sediment transport rate $q_{s,out}$ as

$$q_{s,out}(t) = \frac{NV_p}{LW}\bar{u}_p, \tag{7}$$

where $N(t)$ is the number of particles in the control window $L \times W$ (L is the size in streamwise direction and W corresponds to the flume width), $\bar{u}_p$ is the mean particle velocity in streamwise direction and V_p is the mean particle volume. It is worth noting that this equation provides the averaged transport rate over the window length L. The time resolution of the $q_{s,out}$ series was bounded by the characteristic time that the particles took to cross the window: $t_{tw} = L/\bar{u}_p$. The parameters to be calculated are $N(t)$ and $\bar{u}_p$. The particle activity $N(t)$ was estimated indirectly for each image: we applied a binarisation filter to each image, and we counted the number of pixels characterised by an intensity value over a calibrated threshold. We then considered a calibration factor to convert the pixel number into the particle number $N(t)$. The mean velocity $\bar{u}_p$ was estimated by tracking a set of particles (100–200 grains) in the control window for each experiment. During preliminary tests, we assessed that this measurement technique led to relative error in the average sediment transport rate of less than 10 % when the sampling times were in the 60–120-s range.

2.5 | Bed topography analysis

For each experiment, a bed elevation matrix $Z_0(x,t)$ was computed from the bed profiles collected in the control window. The preliminary step towards the analysis of the bed morphodynamics involved assessing the stability of the bed slope over time. The following step consisted in the subtraction of the mean bed elevation profile from the bed elevation matrix to obtain the bed elevation perturbation matrix $Z(x,t)$. Each matrix $Z(x,t)$ contained information on the morphology and kinematics of the bedform patterns that developed and migrated during the respective run. The typical modes of the perturbations were estimated by applying a 2D fast Fourier transform (FFT) in the wavenumber and frequency domains to the matrix $Z(x,t)$. This operation was equivalent to the application of two consecutive 1D FFT in opposite domain directions. The resulting 2D spectra were analysed to assess the variability of bedform shapes and celerities. Moreover, we tested different scaling schemes to identify general trends in these spectra.

3 | RESULTS

3.1 | Bed elevation perturbations

During the experiments, antidunes developed and migrated upstream along most of the flume length. The bed topography exhibited a nearly constant mean slope over time (Figure 2).

Figure 3 shows one sample of the bed elevation perturbation matrices for each experiment. Antidune behaviour depended on the transport conditions. For example, the antidune patterns migrated more steadily during runs E2 and E3 than during E1. Generally, we observed that antidunes were more uniform and migrated faster for higher sediment feeding rates $q_{s,in}$ (Figure 3). During E1 and E2, antidunes were often observed to develop and migrate as groups of bedforms, also called trains. The number of antidunes composing each train was variable for E1 and E2. These antidune trains were occasionally disturbed or interrupted by local perturbations that propagated downstream. These downstream migrating perturbations were especially visible during E2 (Figure 3(b)) in which they were characterised by typical spacing and period values in the ranges 0.4–0.5 m and 40–50 s, respectively (perturbation velocities around 1 cm s^{-1}). We did not observe any evidence of hydraulic jumps associated with degradation waves. The antidune sequences appeared to be mostly continuous in E3. It is interesting to note that for E4, during which it was difficult to detect antidunes in real time by simple observation, the bed patterns were visible in the corresponding $Z(x,t)$ matrix during most of the run. The $Z(x,t)$ matrix of E4 was characterised by a lower signal-to-noise ratio for the bed profile detection when compared with the other experiments. This signal disturbance was caused by the

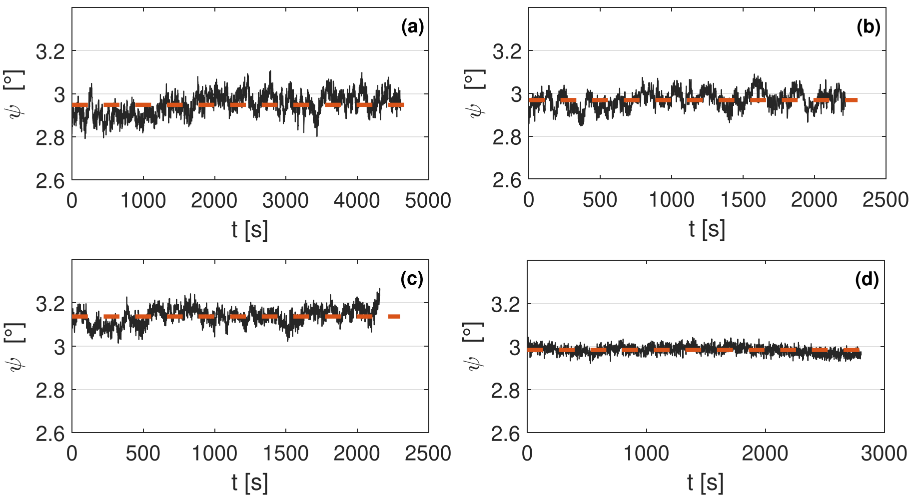

FIGURE 2 Time series of the mean bed slope in the control window for each experiment (black solid lines). Sub-plots from (a) to (d) refer to experiments from E1 to E4, respectively. The red dashed line indicates the mean bed slope over the entire duration of the experiment [Color figure can be viewed at wileyonlinelibrary.com]

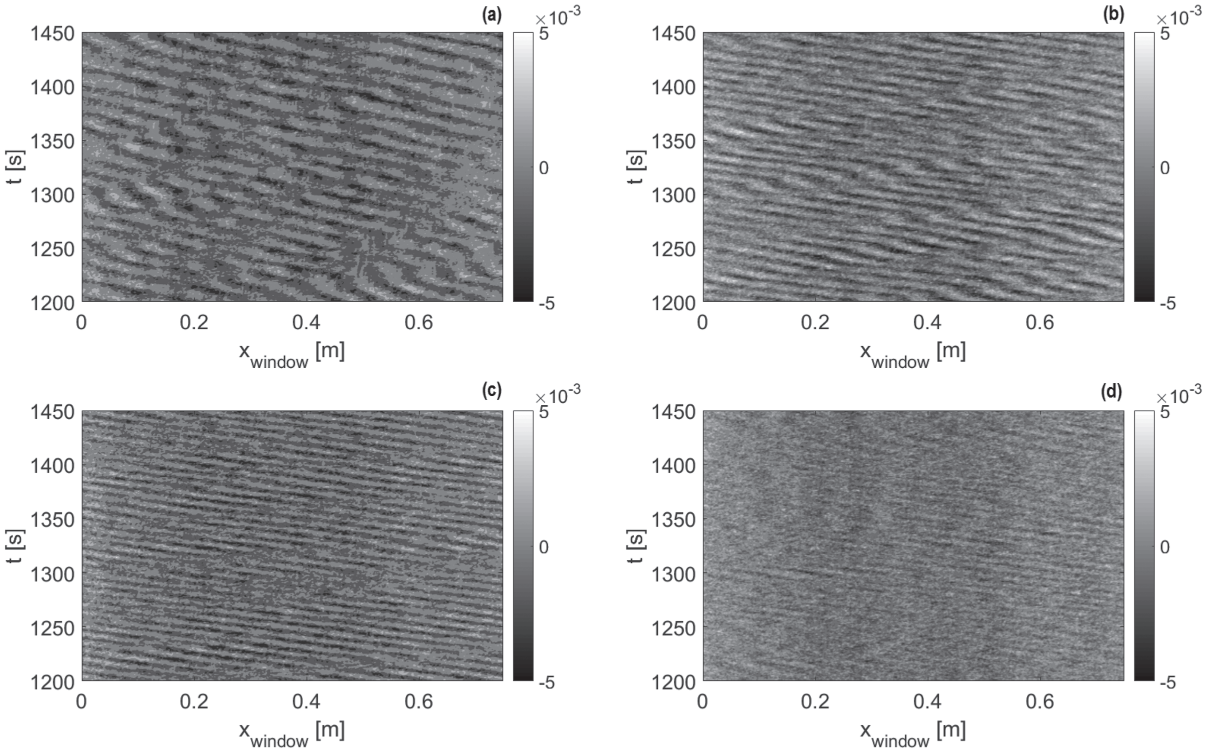

FIGURE 3 Contour plots of the bed elevation perturbation for time intervals of 250 s (from t_1 = 1200 s to t_2 = 1450 s). Sub-plots from (a) to (d) refer to experiments from E1 to E4, respectively. The colour bars refer to the z perturbations expressed as [m]. Sediment feeding rates $q_{s,in}$ were: (E1) $2.0 \cdot 10^{-5}$ m^2 s^{-1}, (E2) $3.5 \cdot 10^{-5}$ m^2 s^{-1}, (E3) $4.8 \cdot 10^{-5}$ m^2 s^{-1}, (E4) $6.1 \cdot 10^{-5}$ m^2 s^{-1}

high particle activity in this run. For all runs, the typical antidune amplitude A ranged from the median grain size d_{50} to the mean flow depth h. The typical antidune wavelengths λ were approximately in the 5–15-mm range. By tracking the bedforms manually, we estimated the migration celerity c for each experiment. Due to the non-uniform migration speed, in particular for E1, the definition of a dominant celerity was considered inappropriate.

3.2 | Bedload transport rate series and fluctuations

The bedload transport rate was measured at the flume outlet throughout the time of the experiment. The resulting time series were characterised by relatively large fluctuations relative to the mean transport rates (Figure 4). Considering the transport rate series averaged over 0.2 s, the highest pulses exceeded the average transport rates by 200 % and 100 % for E1 and E4, respectively. For E1 and E2, episodes of low bedload transport ($q_{s,out}$ < 10 % $\overline{q}_{s,\mathrm{out}}$) at the flume outlet were also recorded. Similar episodes were not observed for E3 and E4. The overall variability of the bedload transport rates, reflected by the coefficient of variation C_v, decreased almost linearly with increasing sediment transport rates (from $C_{v,\,\mathrm{E1}}$ = 0.5 to $C_{v,\,\mathrm{E4}}$ = 0.19).

Bedload transport fluctuations at the flume outlet were likely connected with the antidune morphodynamics. For E1, the antidunes were geometrically well developed, but their migration was particularly unsteady (Figure 3(a)). Consequently, the bedload transport rate at the flume outlet during this run exhibited high variability, reflected by the most remarkable episodes alternating intense and weak

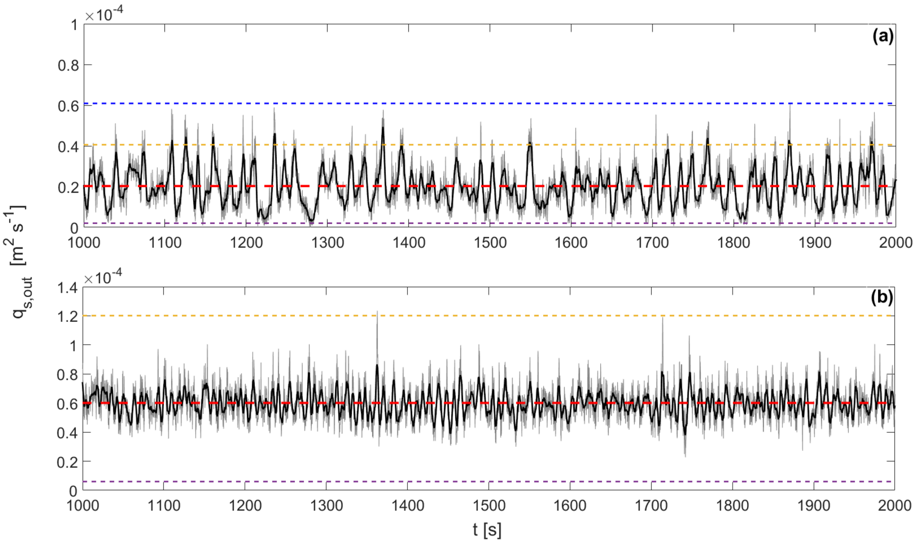

FIGURE 4 Time series of the bedload transport rate at the flume outlet during 1000 s for experiments E1 (a) and E4 (b). The grey solid line indicates the bedload transport rate series averaged over 0.2 s. The black solid line refers to the bedload transport rate averaged over 3 s. The red dashed line indicates the bedload transport rate averaged over the entire duration of the experiment, $\bar{q}_{s,out} \simeq q_{s,in}$. The additional dashed lines represent 2 $q_{s,in}$ (yellow), 3 $q_{s,in}$ (blue), 0.10 $q_{s,in}$ (purple) [Color figure can be viewed at wileyonlinelibrary.com]

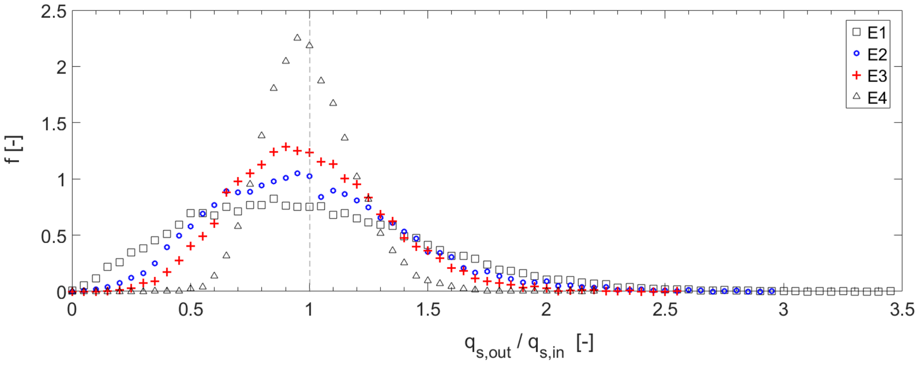

FIGURE 5 Empirical probability density functions for $q_{s,out}/q_{s,in}$ for all the experiments. These distributions refer to the bedload transport rates $q_{s,out}$ averaged over 0.2 s [Color figure can be viewed at wileyonlinelibrary.com]

sediment transport (Figure 5). At intermediate transport stages (E2 and E3), the antidune migration was more regular (Figure 3(b) and (c)) and the fluctuations of $q_{s,out}(t)$ were less intermittent and less strong than for E1 (Figure 5). The bedload transport rates measured in E4 (which is the run with the highest transport intensity) showed the lowest variability, in line with earlier studies (e.g. Singh et al., 2009). The antidune signature was still noticeable in the bed elevation perturbation matrix $Z(x,t)$ for E4 (Figure 3(d)).

3.3 | Spectral analysis of bed morphologies

By applying the 2D fast Fourier transform to the $Z(x,t)$ matrix for each experiment, we obtained the spectra shown in Figure 6 in the λ-T domain. These spectra outlined the multi-scale nature of the bed morphologies and confirmed the observations made by considering only the bed elevation perturbation 2D plots. The FFT technique used did not allow us to determine the migration direction explicitly. In our experiments, antidunes were observed travelling upstream with non-constant geometry and migration celerity. The downstream migrating perturbations (visible in Figure 3(b)) did not appear in these FFT spectra owing to their relatively low energy compared to those associated with the upstream migrating antidunes and their longer migration periods. Additional information regarding the downstream migrating perturbations can be found at the end of the Results section.

To explore and quantify variability in the antidune morphodynamics, we repeated our analysis by considering different domains in the perturbation spectrum. In Figure 6, the power spectral density (PSD) of the bed elevation perturbations in the λ-T domain reveals wavelength variability for each experiment. The wavelength ranged from 0.06 to 0.20 m for E1, and from 0.09 to 0.15 m for E3. Although it was less pronounced than in similar studies on dunes (e.g. Guala et al., 2014), the wavelength variability was nonetheless noticeable in our experiments. This significant variability became less marked with increasing bedload transport intensities.

We also considered the spectra in c-λ plane (Figure 7) to highlight possible trends of migration celerity. Antidune celerity was assumed to take positive values. We transformed the period values T into the corresponding migration celerity values c using the equation

$$c = \frac{\lambda}{T}. \tag{8}$$

Figure 7 shows that migration celerity increased with increasing antidune wavelength for all experiments. Otherwise stated, longer antidunes (high λ) generally migrated upstream faster than shorter ones (low λ). This result appeared consistent with visual analyses of the bed elevation perturbation matrices $Z(x,t)$. The relevance of these observations led us to analyse the spectra in dimensionless domains to determine how the antidune celerity depended on the problem variables. The dimensionless variables (T^*, λ^*, c^*) were obtained by scaling the physical variables (T, λ, c) with the reference flow depth h_0 and the convective time λ/U as characteristic length and time, respectively:

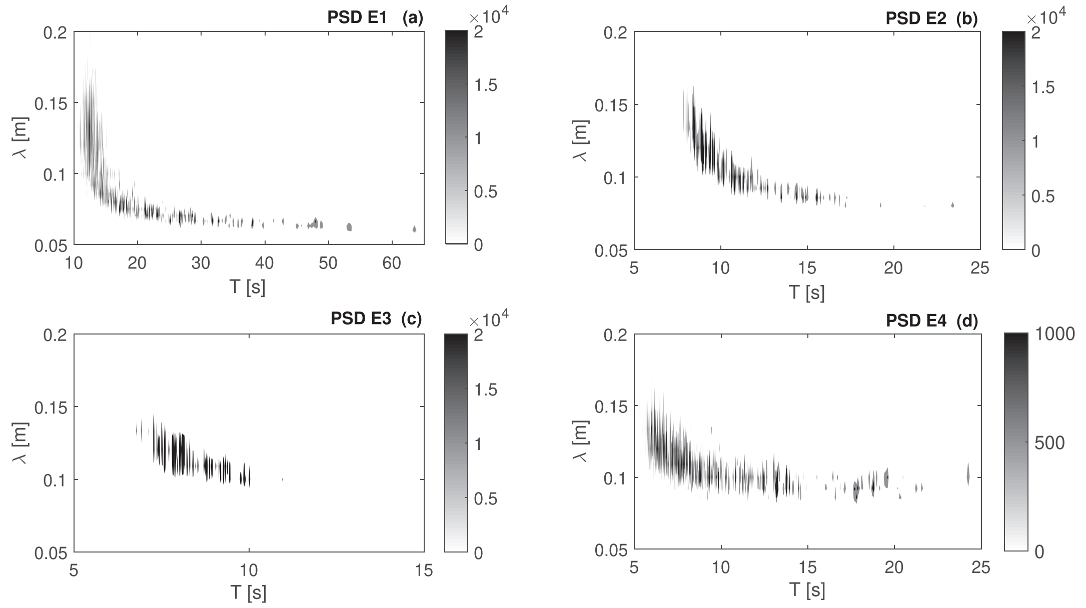

FIGURE 6 Spectra displayed in λ-T domain for experiments E1–E4 (a–d)

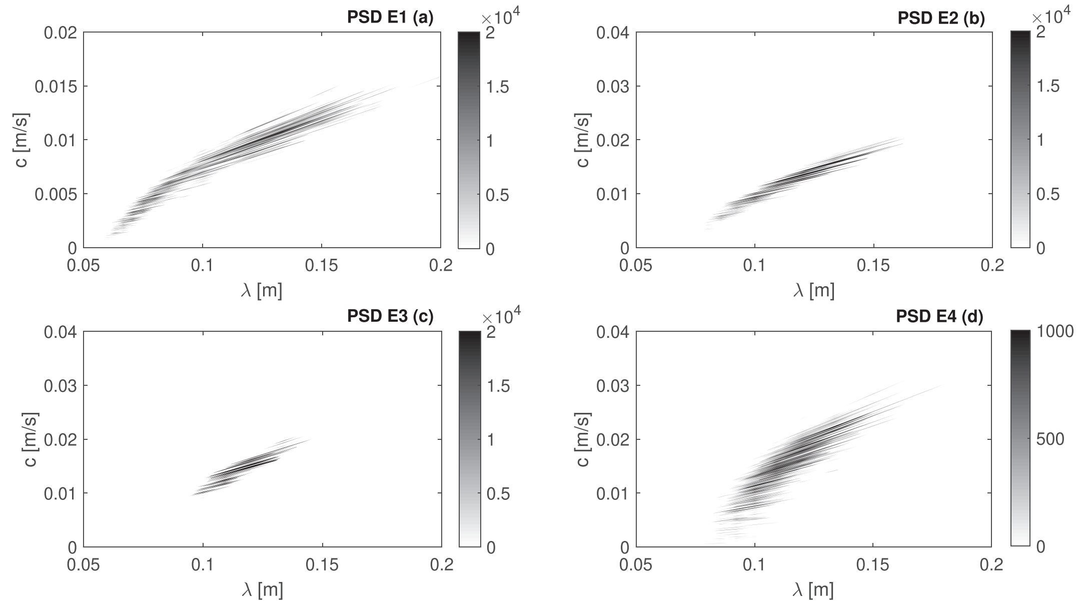

FIGURE 7 Spectra displayed in c-λ domain for experiments E1–E4 (a–d)

$$T^* = T\frac{U}{\lambda}; \tag{9}$$

$$\lambda^* = \frac{\lambda}{h_0}; \tag{10}$$

$$c^* = \frac{c}{U}. \tag{11}$$

Figure 8 shows the contour plots of the spectral densities in c^*-λ^* domain. Note the different criterion used to visualise the E4 PSD contour because this spectrum was characterised by particularly low densities. Interestingly, $c^* \approx f(\lambda^*)$ increased with increasing λ^*, and the higher the transport stage, the steeper the curve $c^* \approx f(\lambda^*)$. Figure 8 also indicates that experiments with the highest transport intensities

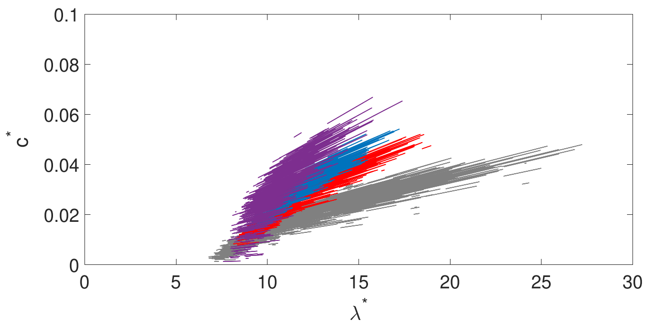

FIGURE 8 PSD contour plot in c*-λ* domain. The colours refer to E1 (black), E2 (red), E3 (blue), E4 (purple). Contours are defined considering a single density level of 5000 for E1–E3. The E4 contour is defined with a density level of 500 [Color figure can be viewed at wileyonlinelibrary.com]

were characterised by the narrowest ranges of dimensionless wavelength.

The dimensionless spectra of the various experiments did not overlap in Figure 8. We believed that the scaling based on the water phase features (Equations (9)–(11)) did not allow us to capture the bedform dynamics in terms of dimensionless celerity and wavelength. In Figure 8, we observed that the mean sediment transport rate likely played a significant role in determining the antidune migration celerity. Based on this observation, we proposed an alternative normalisation scheme. To scale antidune celerity, we defined a characteristic sediment phase velocity U_N:

$$U_\mathrm{N} = \frac{\overline{q}_\mathrm{s}}{d_{\mathrm{V},50}(1-p)}. \tag{12}$$

where p is the porosity of the sediment mixture and $d_{\mathrm{V},50}$ is a characteristic length scale for the mean particle volume V_p (i.e. the diameter of an equivalent sphere of volume V_p). For the sediment mixture used in E1–E4, we measured $p \simeq 0.38$ and $d_{\mathrm{V},50} = (6V_p/\pi)^{1/3} \simeq 2.4$ mm. U_N is proportional to the virtual convective velocity of the sediment volume in the bed active layer—whose mean thickness was assumed proportional to the characteristic grain size. This assumption is in agreement with the typical antidune amplitude observed in our experiments. We calculated the scaled dimensionless migration celerity c_N^* as

$$c_\mathrm{N}^* = \frac{c}{U_\mathrm{N}} = \frac{c\,d_{\mathrm{V},50}(1-p)}{\overline{q}_\mathrm{s}}. \tag{13}$$

Regarding the wavelength scaling, we considered the relationship proposed by Recking et al. (2009) to predict the dominant antidune wavelength on steep slopes:

$$\lambda_{\mathrm{R09}} = d_{50} f(\Theta,\Theta_\mathrm{c},Fr) = d_{50}\,\xi\left(\Theta^\alpha \Theta_\mathrm{c}^\beta Fr^\gamma\right) = 0.093\Theta\Theta_\mathrm{c}^{-3} Fr d_{50}. \tag{14}$$

The combination of parameters in Equation (14) was the result of detailed dimensional analysis conducted using Buckingham's Pi theorem; the coefficients $(\xi,\alpha,\beta,\gamma)$ were determined by fitting the relationship to data derived from 19 flume experiments (Recking et al., 2009). This validated relationship appeared well suited to be tested as the wavelength reference scale for antidunes on steep slopes. We defined the dimensionless wavelength values λ_N^* as

$$\lambda_\mathrm{N}^* = \frac{\lambda}{\xi\Theta\Theta_\mathrm{c}^{-3} Fr d_{50}} = \frac{\lambda}{\lambda_{\mathrm{R09}}}. \tag{15}$$

The coefficient $\xi = 0.093$ [-] was not strictly required for the wavelength scaling, but maintaining it eased the interpretation of the λ_N^* values in proportion to λ_{R09}. Figure 9 shows the resulting contour plots for the spectra in the c_N^*-λ_N^* domain.

This scaling based on the parameters U_N and λ_{R09} allowed us to collapse all the spectral distributions onto a master curve $c_\mathrm{N}^* \approx f(\lambda_\mathrm{N}^*)$. The spectrum obtained for E4 followed the same trend; we plotted it separately in Figure 9(b) for the sake of readability. Based on the trend of the spectral distributions in Figure 9, we expressed the relationship between scaled dimensionless celerity c_N^* and dimensionless wavelength λ_N^* as

$$c_\mathrm{N}^* \approx f(\lambda_\mathrm{N}^*) = \frac{(\lambda_\mathrm{N}^* - \lambda_\mathrm{A}^*)^\zeta}{k}, \tag{16}$$

where $\lambda_\mathrm{A}^* \simeq 0.57$ [-], $\zeta \simeq 2/3$ [-] and $k \simeq 1$ [-] are regression coefficients.

By combining Equation (16) and Equation (13), we obtained an explicit formula to estimate the mean bedload transport rate associated with upstream migrating antidunes:

$$\overline{q}_{\mathrm{s,est}} = c\,d_{\mathrm{V},50}(1-p) f_\mathrm{q}(\lambda_\mathrm{N}^*) = c\,d_{\mathrm{V},50}(1-p)\left[\frac{1}{(\lambda_\mathrm{N}^* - 0.57)^{2/3}}\right], \tag{17}$$

where $f_\mathrm{q}(\lambda_\mathrm{N}^*) = [f(\lambda_\mathrm{N}^*)]^{-1}$. Equation (17) shares some similarity with the frameworks proposed for downstream migrating dunes (e.g. Guala et al., 2014; Nikora, 1984; Simons et al., 1965) and differs in other aspects. These features are discussed in the Discussion section.

3.3.1 | Performance assessment of Equation (17) with data available in literature

Although Equation (17) is based on the approximation underpinning Equation (16), it can be used to estimate the mean bedload transport rate by measuring the typical wavelength and associated celerity values for antidunes migrating upstream along steep slopes. We first assessed the performance of this approach to estimate the average bedload discharge. To that end, we used data from an experiment on antidunes obtained by Mettra (2014), who set the values listed in Table 3 for the mean bed slope $\overline{\psi}$, the flume width W and the sediment size d_{50}. Mettra (2014) observed upstream migrating antidunes and applied a tracking criterion based on longitudinal bed profiles to collect wavelength and celerity data.

To run this test, we first estimated the corresponding λ_N^* values from the λ values reported in Table 3 ($\lambda_{\mathrm{R09}} = 0.257$ m for this experiment). The Shields number Θ was calculated using Equation (1) with R_b estimated according to the Einstein–Johnson method as for the experiments presented here. The critical Shields number Θ_c was calculated using Equation (6). We calculated the U_N and c_N^* values according to Equation (12) and Equation (13). Since the information about the mean particle volume was not available for the run *2deg15v*, we indirectly estimated $d_{\mathrm{V},50}$ assuming the same ratio $d_{\mathrm{V},50}/d_{50} = 0.83$ obtained for our experimental case. The porosity of the sediment mixture was $p = 0.42$ (Mettra, 2014). We then used Equation (17) to calculate the corresponding $\overline{q}_{\mathrm{s,est}}$ values (Table 4). Figure 10 shows the 'true' positions of the pairs (c_N^*, λ_N^*) computed from the mean bedload transport rate $\overline{q}_{\mathrm{s,meas}}$ (measured during the experiment). Since the maximum relative error for the mean bedload transport estimates was less than 20 %, the outcome of the test appeared satisfactory. This test highlighted the importance of having multiple pairs (c,λ) or better the c-λ spectrum to assess and improve the reliability of the results. Unfortunately, we had to limit the comparison to a single experimental case because of the scarcity of experimental data available in the literature (in terms of associated values c and λ) for antidunes on steep streams with coarse sediments.

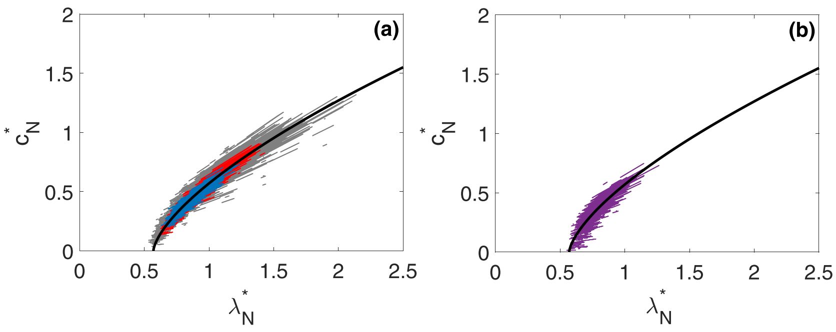

FIGURE 9 PSD contour plots in c_N^*-λ_N^* domain. The black lines represent the master curve of Equation (16). (a) The colours refer to: E1 (grey), E2 (red), E3 (blue). Contours are defined considering a single density level of 5000 for E1–E3. (b) The E4 contour (purple) is defined with a density level of 500 [Color figure can be viewed at wileyonlinelibrary.com]

TABLE 3 Main parameters of the experimental run 2deg15v (Mettra, 2014) and pairs (c,λ) based on data of the same experiment

W [m]	$\overline{\psi}$ [°]	d_{50} [mm]	ρ_s [kg m^{-3}]	h [m]	Fr [-]	R_b [m]	Θ [-]	c [mm s^{-1}]	λ [m]
0.08	2.0	6.25	2690	0.027	1.17	0.024	0.08	0.8	0.20
								1.8	0.30
								2.5	0.40

Note. The pairs (c, λ) were extracted from Figure 6.6 and Figure 6.8 (a) in Mettra (2014).

TABLE 4 Summary of the performance assessment of Equation (17) for the run 2deg15v (Mettra, 2014)

c [mm s^{-1}]	λ [m]	λ_N^* [-]	$\overline{q}_{s,meas}$ [m^2 s^{-1}]	$\overline{q}_{s,est}$ [m^2 s^{-1}]	$(\overline{q}_{s,est}-\overline{q}_{s,meas})/\overline{q}_{s,meas}$ [%]
0.8	0.20	0.78	$7.9 \cdot 10^{-6}$	$6.43 \cdot 10^{-6}$	−18.0
1.8	0.30	1.17		$7.64 \cdot 10^{-6}$	−2.7
2.5	0.40	1.56		$7.60 \cdot 10^{-6}$	−3.3

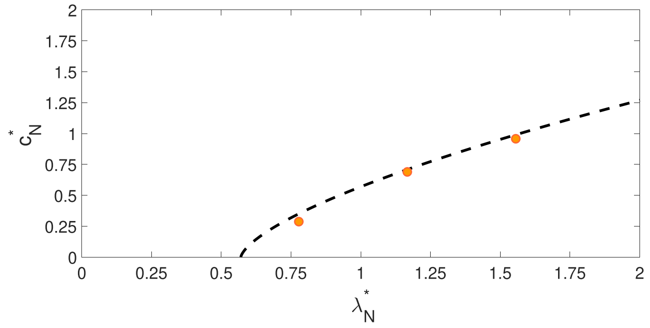

FIGURE 10 Master curve of Equation (16) (dashed black line). The orange circles display the positions in c_N^*-λ_N^* domain of the data pairs reported in Table 3 for the run *2deg15v* (Mettra, 2014). The pairs (c_N^*, λ_N^*) were calculated considering the $\overline{q}_{s,meas}$ value measured by Mettra (2014) and reported in Table 4 [Color figure can be viewed at wileyonlinelibrary.com]

3.3.2 | Domain of application of Equations (16) and (17)

We provide here further guidance on how to apply Equations (16) and (17). The data from which these relationships were derived came from experiments characterised by high relative roughnesses and steep slopes ($\overline{\psi}$ = 3°). The scaling analysis presented above holds for supercritical flows over well-sorted coarse natural sediments (i.e. $d_{50}/h \approx$ 0.1–0.5 and $d_{50} \approx$ 2–10 mm). Equation (16) is valid for mean slope angles $\overline{\psi}$ up to ~4°, provided the flow remains supercritical over most of the flume length and the bed shows no significant ψ fluctuations on the flume scale. Mettra (2014) observed degradation waves in one steep-slope experiment ($\psi \approx 4°$) and suggested the metastability of the bed profile as a potential cause. Concerning streams under near-critical flow conditions ($Fr \sim 1$), we recommend to carefully assess the continuity of the upstream migrating antidune pattern in the control window (recall Figure 3 and Figure 11). Equation (16) is not expected to hold in the presence of extensive discontinuities in the antidune sequences (e.g. sediment waves or transitional bedforms). During an experimental run conducted with the same flume and sediments of the present study (with $\overline{\psi}$= 1.55° and Fr = 1.1), Ancey and Pascal (2020) observed bed waves—characterised by 'cycles of growth and decay over time scales of a few minutes, with no evidence of migration'—in the upstream part of the flume (see Movie S2 in the same paper), whilst upstream migrating antidunes were well developed in the downstream part. A plastic plate was installed over the flow surface in the middle part of the flume to facilitate particle tracking; this disturbance probably influenced the bedforms (Ancey & Pascal, 2020). In that specific configuration, the bed morphodynamics in the upstream sector was not consistent with the application domain of Equation (16). With regard to bedload transport intensity, the experimental conditions of E4 likely represent the upper boundary when applying Equation (17) to estimate the mean bedload transport rate. The cases characterised by very low bedload transport rates require special attention because, in such circumstances, bedload transport is intermittent, and this intermittency affects antidune migration.

3.4 | About the downstream travelling perturbations

We provide here additional information regarding the downstream travelling perturbations of the antidune sequences observed in our

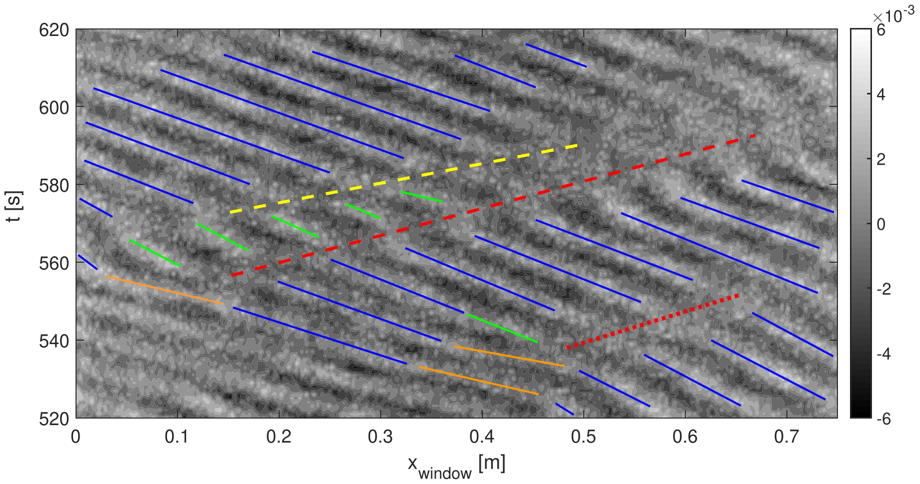

FIGURE 11 Contour plot of the bed elevation perturbation $Z(x, t)$ during E2 (100 s). The solid blue lines represent the approximated crest trajectory of undisturbed antidunes. The solid orange lines indicate the accelerating antidunes, whereas the green lines indicate new antidune crests resulting from splitting events or disturbance-related discontinuities. The other thick lines represent a travelling disturbance with discontinuity of the antidune pattern (long-dashed red), a splitting-related disturbance without persistent discontinuity (short-dashed red) and a secondary discontinuity/rearrangement of the antidune pattern (long-dashed yellow) associated with a previous discontinuity. The colour bar refers to the z perturbation expressed as [m] [Color figure can be viewed at wileyonlinelibrary.com]

experiments. These observations might be useful for researchers who study morphodynamic instabilities in supercritical flows. The perturbations on which we focus here (also called 'disturbances' in the previous sections) were downstream travelling discontinuities or non-uniformities in the wave geometry and celerity that affected the antidune sequences in our experiments. Looking at the E2 contour plot in Figure 11, one can identify perturbations which interrupt or not the antidune pattern continuity. For instance, we observed downstream travelling perturbations which propagated from accelerating antidunes. These perturbations were often associated with the splitting of one accelerating antidune or the appearance of a transition zone—likely an area with high particle activity—in which one could not distinguish the bedform crests and troughs that were previously evident (Figure 11). In other cases, we observed occurrences of a local slowdown of one antidune that subsequently propagated downstream affecting other antidunes. The perturbations travelled with typical celerity values of the same order of magnitude of the antidune celerity. This observation suggests a strong link with the bedload transport intensity. The travelling perturbations can also be interpreted as boundaries between the antidune trains when they were long lasting. These types of perturbations and trains were mostly evident and frequent during the experiments characterised by the lowest mean bedload transport rates (E1 and E2). Note that these trains did not vanish (or break suddenly), and apparently the flow remained supercritical over the entire flume length.

Although the width of the control window in our experiments prevented the systematic analysis of the length and time scales of these downstream travelling perturbations, our experimental setup allowed us to make some interesting observation regarding the persistence of these perturbations in the time and space domains. Sometimes, these perturbations came from upstream and travelled across the entire control window. In other cases, they seemed to originate from a local event in the antidune sequence (e.g. the sudden acceleration of a single antidune or an antidune splitting), and they propagated downstream. We also observed travelling disturbances which caused a marked discontinuity in the antidune pattern (i.e. the transition zones mentioned above), and that were apparently damped (diffused?) over distances of few tens of centimetres (Figure 11).

4 | DISCUSSION

As presented in the previous sections, the antidunes observed during the experimental runs exhibited significant variability of their wavelength and migration celerity. The wavelength variability was found to be less pronounced for the experiments characterised by higher mean sediment transport rate. To the best of our knowledge, the range of variability for the antidune wavelength on a steep slope under moderate and intense bedload transport conditions has so far never been specified. This result was made possible by the application of spectral analysis on high-resolution data. Looking at the bed elevation perturbation profiles, the antidunes were less prone to amplitude variability. The typical antidune amplitudes were observed to be slightly smaller than the mean flow depth. Regarding the antidune migration celerity, its variability was also noticeable and antidune celerity increased with increasing wavelength. Overall, antidunes characterised by similar wavelength values migrated faster for higher mean bedload transport rate.

In the next section, we discuss the factors that could cause the variability of antidune morphodynamics observed in our experiments. We then explore the potential implications for related topics, such as the estimation of a friction term associated with antidunes in flows characterised by high relative roughness and the links between antidune morphodynamics and sediment transport regimes.

4.1 | Antidune morphodynamics and implications

We summarised the λ ranges for the experimental runs E1–E3 in Table 5. To add an element of comparison in Table 5, we reported the

TABLE 5 Summary of the ranges for the antidune wavelength λ (extracted from the spectral distributions) and estimated values for $\lambda_{\mathrm{min\,K63}}$ (Equation (18) considering $\overline{h} = h_0$) and λ_{R09} (Equation (14)) (runs E1–E3)

Run	λ [m]	λ_{minK63} [m]	λ_{R09} [m]
E1	0.06–0.20	0.09	0.106
E2	0.08–0.16	0.11	0.122
E3	0.09–0.15	0.124	0.133

wavelength $\lambda_{\mathrm{min\,K63}}$ and λ_{R09} computed for each experiment. $\lambda_{\mathrm{min\,K63}}$ is the theoretical minimum wavelength for 2D antidunes, according to Kennedy (1963), as

$$\lambda_{\mathrm{min\,K63}} = 2\pi Fr^2 \overline{h}. \tag{18}$$

As presented in Table 5, Equation (14) might provide good estimates of the mean antidune wavelength for E1 and E2. The λ_{R09} value estimated for E3 is closer to the maximum wavelength value. However, it is important to recall that this empirical equation was formulated to estimate the dominant antidune wavelength, and its fitting was based on flume data for which the wavelength values were determined by dividing the length of the observation window by the number of antidunes detected (Recking et al., 2009).

Interestingly, the comparison of the values of $\lambda_{\mathrm{min\,K63}}$ with the ranges of λ determined from the spectra indicates that the shortest waves detected using 2D FFT were located in the region of existence of 3D antidunes according to Kennedy's stability diagram (Kennedy, 1963). This observation indicates that upstream migrating 2D antidunes (also named *long-crested*) and 3D antidunes might coexist and interact in supercritical flows over steep slopes, contributing to the variability of antidune shapes and celerities. This speculation could be a possible interpretation for the non-linear trends of the relationship between dimensionless migration celerity and dimensionless wavelength in Figure 8 and Figure 9. The real-time observation of the flow free surface over short antidunes in our experiments revealed transversal wavelets but without evidence of roaster tails. The wave amplitude of these wavelets was noticeably smaller than that of the water surface undulations caused by the sinusoidal bedforms. Regarding the bed shape for the short antidunes in our experiments, we sporadically observed antidune troughs that were more pronounced on the flume centreline than close to the flume walls, but the crests appeared 2D. These kinds of short bedforms might thus be typical of very shallow supercritical flows in which the particular conditions—notably the high relative roughness—might influence their form, shaping them differently from the 3D *short-crested* antidunes reported by other authors for flows characterised by lower relative roughness values (e.g. Kennedy, 1963). The small flume width values in our study, in the experiments conducted by Mettra (2014) and in some of the runs presented by Recking et al. (2009), might also play a role in the morphodynamics of these short antidunes in terms of lateral confinement. Inoue et al. (2020) recently investigated the coexistence of 3D antidunes with alternate bars. Additional experimental studies considering different relative roughness d_{50}/h and aspect ratio h/W values—with systematic monitoring of the sediment transport and flow conditions—would be useful to further clarify the mechanisms that control the coexistence of different bedforms in supercritical flows over coarse-bedded streams.

At the meso-scale, a possible mechanism that may exacerbate variability in antidune geometry and celerity is related to the interactions within antidune trains which can involve antidunes of various wavelengths, but with similar amplitudes. These non-linear interactions often have the capacity to cause neighbouring antidunes to rearrange. Examples of this phenomenon can be observed in the contour plots of the bed elevation perturbation for E1 (Figure 3 (a)) and E2 (Figure 11), and in Movie S1 (Supporting Information). Antidune interactions can be interpreted phenomenologically using the *lag distance* concept (Kennedy, 1963). Even small particle clusters eroded or deposited within a short time interval can have strong impacts on local flow and transport conditions. The effects of these perturbations are likely accentuated by the high relative roughness of the flows under study. In particular, in steep streams, an increase in the particle activity can trigger collective entrainment, that is, the dislodgement of several particles at the same time (Heyman et al., 2016). Consequently, the local lag between sediment flux and shear stress can be impacted non-uniformly by these bedload bursts along the stream. As a result, antidunes exhibiting similar geometries can be perturbed, undergo a non-uniform change in their migration celerity and coalesce (or split), producing longer (or shorter) antidunes, as was observed for instance in run E1 (Figure 3 (a) and Movie S1) and run E2 (Figure 11). Interestingly, these events were observed mainly during E1, less frequently during E2 and were less clearly identifiable during E3 and E4. This is consistent with the fact that local bedload transport pulses (or, conversely, phases of weak transport) are more frequently observed under low bedload transport conditions than under intense transport (Singh et al., 2009).

The formation, development and evolution of trains composed of a number of well-developed antidunes was likely caused by the above-mentioned interactions. Similar morphological patterns have been observed in experiments and the field (e.g. Froude et al., 2017; Recking et al., 2009), and their appearance likely represents a distinctive feature of the variability of antidune morphodynamics on steep slopes. According to Grant (1994), antidune interaction within these trains promotes an increase in the antidune wavelength, which could explain step–pool formation. Similar antidune trains have also been reproduced in numerical simulations by Bohorquez and Ancey (2016), who regarded 'nonlinear coarsening' as a possible cause of the antidune wavelength increase observed in the upstream migration process.

The downstream travelling perturbations already described in the Results section can be interpreted as a complementary feature of the antidune trains. These disturbances either appear as the transient signature of local interactions (e.g. bedform merging and splitting events) or they mark a more persistent discontinuity in the antidune pattern and thus can be considered as boundaries between the antidune trains. We also tried to investigate the possible influences of these disturbances on the bedload transport rate series measured at the flume outlet. Assuming a constant perturbation celerity, we inferred the arrival times at the flume outlet of the perturbations that travelled across the control window. Unfortunately, we did not succeed in identifying a clear correlation between the estimated arrival times of these downstream migrating perturbations at the outlet and the occurrences of bedload pulses or phases of weak transport. The simple assumption of a constant perturbation celerity in the downstream part of the flume in which the antidunes are close to the outlet discontinuity is probably not sufficient to extrapolate a correspondence between perturbations and bedload pulses.

In our experiments of bedload transport over steep slope, antidune train morphodynamics likely depends on how particle diffusivity and deposition (governed by local flow conditions) and entrainment (strictly related to particle activity) are interrelated (Ancey & Heyman, 2014; Bohorquez & Ancey, 2016; Heyman et al., 2016). The parts played by the absolute nature of the antidune instability (Vesipa et al., 2014) and by turbulence (Breakspear, 2008) may be crucial as well. In steep stream flows under moderately intense transport conditions (as in E1 and E2), investigating these interrelations remains a great challenge because we need to (i) track not only isolated particles but also particle clusters when measuring particle diffusivity, (ii) run particle image velocimetry (PIV) in difficult conditions and (iii) monitor antidune evolution at high temporal and spatial resolution. Further studies on these interrelated processes are needed to confirm or infirm the possible influence of processes located far upstream (such as the sediment supply irregularities) on bedload transport in steep streams (Ancey et al., 2015; Furbish & Roering, 2013; Heyman et al., 2016; Tucker & Bradley, 2010), and their impact on bed instabilities.

Variability in the antidune morphodynamical features may affect flow resistance induced by antidunes. For flows on rough beds (that is, under low submergence conditions), the relative importance of grain- and form-induced flow resistance depends a great deal on antidune shape variability, in particular on the non-uniform and abrupt changes in bed curvature that may be caused by erosion or deposition of a relatively small number of grains. Bed curvature alters the momentum distribution within the flow (Dressler & Yevjevich, 1984). It has been taken into account for a sinusoidal bed surface by Vesipa et al. (2012), who used the Dressler equations (Dressler, 1978)—rather than the common form of the Saint-Venant equations—and a mechanistic model for sediment transport. Our experimental results and analyses prove that form-induced flow resistance may be neglected to estimate the double-averaged flow depth $\langle \overline{h} \rangle$ and to describe the typical bedform dynamics when considering relatively continuous antidune trains. However, the experimental observation of transient local non-uniformities (e.g. antidune merging and splitting events) and of downstream travelling perturbations which propagated from one or two accelerating antidunes (Figure 11) should spur further research on the interplay between curvature-induced flow resistance and antidune morphodynamics variability by taking a closer look at factors such as interaction between bedforms, the influence of the bedload transport stochastic nature and the perturbations caused by turbulence and unsteady sediment supply.

The present study explains why antidunes are seldom directly observed in the field and possibly why geomorphological records of natural gravel-bed streams may be difficult to interpret even when antidunes were not strongly reworked by later events. Direct observation is made difficult by the antidune geometry and celerity variability, which can thus ‘hide’ their presence during flood events. Even in field sites for which disturbing factors such as grain sorting play a minor role, antidune trains are less visible than expected because of variability. In this respect, with the advent of cost-effective drone-based technologies (e.g. UAV-carried multi-beam sonar and ground penetrating radar) we expect a revival of interest in the field investigations on antidunes. Our experimental work is a first step towards determining the variability ranges in the antidune geometry and celerity.

4.2 | The interplay between transport intensity and upstream migration celerity

In the Results section, we demonstrated that the celerity scaling based on U_N is useful to model how the sediment flux affects the antidune migration. As expected, the larger the mean sediment flux, the higher the migration celerity c. The intense particle activity promotes deposition on the antidune stoss side, and erosion on its lee side. We now compare the structure of Equation (17) with that of the formula (Equation (19)) originally proposed by Simons et al. (1965) to model the contribution of downstream migrating dunes to the bedload flux.

$$\overline{q}_s = (1-p)\, d_{V,50}\, f_q\left(\lambda_N^*\right) c = \frac{1}{2}(1-p)\left(2 d_{V,50}\right) f_q\left(\lambda_N^*\right) c \qquad (17)$$

$$\overline{q}_s = \frac{1}{2}(1-p)\, H_{dune}\, c_{dune} + C_{q,1} \qquad (19)$$

As one can see in the two equations reported above, Equation (17) might also be interpreted as a ‘contribution’ to the mean bedload flux of a triangular antidune with the same shape coefficient $\left(\frac{1}{2}(1-p)\right)$ of the Simons' formula. Analogously, the term $2\,d_{V,50}$ is proportional to the bedform amplitude (H_{dune} is the dune amplitude). The migration celerities also appear in both Equation (17) and Equation (19). It is worth noting that the celerity of upstream migrating antidunes takes positive values in our framework, whereas the sign convention is different in Equation (19) (celerity $c_{dune} > 0$ for downstream migrating dunes). The term $C_{q,1}$ in Equation (19) is a constant of integration that stands for the ‘part of the bedload which does not enter into propagation of dunes and ripples’ (with $C_{q,1} = 0$ at the threshold of motion and as long as the bed is covered by dunes, and $C_{q,1} = \overline{q}_s$ in case of transport in plane bed configuration) (Simons et al., 1965). Some hypotheses concerning the possible values taken by the ‘shape factor’ (not formally defined) were already formulated by Mettra (2014) for the bedload flux contribution of a single antidune. The main difference between the relationships proposed for uni- and multi-modal dune fields (e.g. Guala et al., 2014; Nikora, 1984; Simons et al., 1965) and Equation (17) is that the latter should not be intended as the integral of the bedload flux contributions resulting from multiple migrating bedforms of different geometry. This semi-empirical multi-scale relationship for estimating the mean bedload transport rate is based on the meaning of Equation (16): an upstream migrating antidune within an antidune sequence under quasi-equilibrium transport conditions typically responds to the forcing imposed by the mean bedload transport rate $\overline{q}_s$ by migrating with celerity proportional to U_N and to $f\left(\lambda_N^*\right)$. According to our results, antidune upstream migration may be formally interpreted as a response to the mean bedload flux and not as a contribution to it. The functional form of the dimensionless wavelength $f\left(\lambda_N^*\right) = \left[f_q\left(\lambda_N^*\right)\right]^{-1}$ in Equation (16) embeds the effects on the migration celerity of both antidune shape and mean flow conditions (see Equation (14)). The term $f\left(\lambda_N^*\right)$ in Equation (16) can be interpreted as an empirical conversion factor that expresses the typical ratio of the mean bedload flux that actively participates in determining the migration celerity of antidunes characterised by a dimensionless wavelength λ_N^* (depositing on their stoss side and being eroded by their lee side). The positive trend for $f(\lambda_N^*)$ likely reflects the signature of the damping effect induced by the bedload layer inertia on antidune migration. In fact, inertial effect can increase the lag between sediment flux and shear stress, slowing antidune migration. The negative impact of inertia on the antidune migration celerity has been demonstrated theoretically by Vesipa et al. (2012). It seems coherent that this damping effect impacts relatively more the migration celerity of the short antidunes than that of the long ones because of their different size, thus causing the non-linearity in $f(\lambda_N^*)$. According to our observations, the interplay between sediment flux and inertia may hold at relatively high transport rates (E4) until the situation in which the antidunes are levelled out (bedload-laden flow with not clearly identifiable bed-flow interface). Considering the PSD contour for E1 in Figure 9(a), $f(\lambda_N^*)$ may take values higher than the unity. This somewhat unexpected outcome might suggest that the longest antidunes during E1 migrated under sustained bedload transport rate higher than the mean feeding rate (i.e. during long-lasting bedload pulses) and/or that their actual wave amplitude was lower than $2d_{V,50}$. However, in our experiments, we did not find any clear proportionality between the antidune amplitude and wavelength. It is worth underlining that the scaling method presented in this paper is based on parameters that have been estimated by considering relationships holding for uniform flows. This method has proven to be successful for describing the typical morphodynamic features observed in our experiments; alternative approaches, which take flow non-uniformity into account, could reveal interesting information concerning particular local events such as bedload pulses associated with the migration of a single antidune or to the transit of a downstream travelling perturbation.

5 | CONCLUSION

The experimental study presented in this paper shows that antidunes on steep slopes exhibit significant variability of shapes and celerity, even under steady-state conditions. The wavelength variability range increased with decreasing mean sediment transport rate. Overall, we observed that the larger the antidune wavelength, the higher its migration celerity. One strength of this paper is that it shows how to infer information on this variability from high-resolution data by applying spectral analysis. By using a scaling technique, we collapsed all the bed elevation perturbation spectra onto a single curve that captured the bedform dynamics in terms of dimensionless celerity c_N^* and wavelength λ_N^*. The resulting trend $c_N^* \approx f(\lambda_N^*)$ was described by a functional relationship. This multi-scale relationship embedded the interplay between the sediment flux and antidune migration. We proposed a new method for estimating the mean bedload transport rate by monitoring antidune morphodynamics. Although our first test gave satisfactory results, additional data are needed to confirm our results. We are currently conducting a new experimental campaign using a longer flume.

Accounting for variability in the antidune morphodynamical features is key to estimating sediment fluxes and form-induced flow resistance on steep slopes. This variability likely explains the elusiveness of antidunes in direct field observations. The findings may help paleohydraulics studies regarding coarse-bedded streams.

ACKNOWLEDGEMENTS

P.B. was supported by the Spanish Ministry of Science, Innovation and Universities (MICINN/FEDER, UE) under Grant CGL2015-70736-R. We thank Dr. François Mettra for all discussions related to his data. Note also that he built the former version of the flume that we used for our experiments. We thank Gaëtan Gindrat for his contribution to the experimental work during his semester project with us. We are grateful to Dr. Gauthier Rousseau for the fruitful exchanges concerning the experimental setup. We thank Dr. Matthieu Cartigny and the Associate Editor for the constructive comments that have contributed to improving the paper.

CONFLICT OF INTEREST

The authors declare that there are no conflicts of interest that might be perceived as influencing the authors' objectivity and the impartiality of the research presented.

DATA AVAILABILITY STATEMENT

The data that support the findings of this study are available in the supplementary material of this article. Bed topography data are available in Supporting Information S2. Bedload transport data are available in Supporting Information S3.

ORCID

Ivan Pascal https://orcid.org/0000-0001-6599-6222
Christophe Ancey https://orcid.org/0000-0003-3354-7398

REFERENCES

Alexander, J. (2008) Bedforms in Froude-supercritical flow. *Marine and River Dune Dynamics 1-3 April 2008 Proceedings*. Leeds, UK: University of Leeds, pp. 1–5.

Ancey, C., Bohorquez, P. & Heyman, J. (2015) Stochastic interpretation of the advection diffusion equation and its relevance to bed load transport. *Journal of Geophysical Research: Earth Surface*, 120, 2529–2551.

Ancey, C. & Heyman, J. (2014) A microstructural approach to bed load transport: mean behaviour and fluctuations of particle transport rates. *Journal of Fluid Mechanics*, 744, 129–168.

Ancey, C. & Pascal, I. (2020) Estimating mean bedload transport rates and their uncertainty. *Journal of Geophysical Research: Earth Surface*, 125, e2020JF005534.

Andreotti, B., Claudin, P., Devauchelle, O., Durán, O. & Fourrière, A. (2012) Bedforms in a turbulent stream: ripples, chevrons and antidunes. *Journal of Fluid Mechanics*, 690, 94–128.

Bohorquez, P. & Ancey, C. (2016) Particle diffusion in non-equilibrium bedload transport simulations. *Applied Mathematical Modelling*, 40, 7474–7492.

Bohorquez, P., Cañada Pereira, P., Jimenez-Ruiz, P.J. & del Moral-Erencia, J.D. (2019) The fascination of a shallow-water theory for the formation of megaflood-scale dunes and antidunes. *Earth-Science Reviews*, 193, 91–108.

Bose, S.K. & Dey, S. (2009) Reynolds averaged theory of turbulent shear flows over undulating beds and formation of sand waves. *Physical Review E*, 80(3), 36304.

Breakspear, R. (2008) Hydrodynamics and sedimentary structures of antidunes in gravel and sand mixtures. Ph.D. Thesis, University of Southampton.

Cao, H.H. (1985) Résistance hydraulique d'un lit de gravier mobile à pente raide étude expérimentale. Ph.D. Thesis, École Polytechnique Fédérale de Lausanne.

Carling, P.A., Burr, D.M., Johnsen, T.F. & Brennand, T.A. (2009) A review of open-channel megaflood depositional landforms on Earth and Mars. In: Burr, D., Carling, P., Baker, V. (Eds.) *Megaflooding on Earth and Mars*. Cambridge, UK: Cambridge University Press, pp. 33–49.

Carling, P.A. & Shvidchenko, A.B. (2002) A consideration of the dune: antidune transition in fine gravel. *Sedimentology*, 49(6), 1269–1282.

Cartigny, M.J.B., Ventra, D., Postma, G. & Den Berg, J.H. (2014) Morphodynamics and sedimentary structures of bedforms under supercritical-flow conditions: new insights from flume experiments. *Sedimentology*, 61, 712–748.

Chin, A. (1999) The morphologic structure of step-pools in mountain streams. *Geomorphology*, 27(3), 191–204.

Coleman, S.E. & Fenton, J.D. (2000) Potential-flow instability theory and alluvial stream bed forms. *Journal of Fluid Mechanics*, 418, 101–117.

Colombini, M. (2004) Revisiting the linear theory of sand dune formation. *Journal of Fluid Mechanics*, 502, 1–16.

Colombini, M. & Stocchino, A. (2005) Coupling or decoupling bed and flow dynamics: fast and slow sediment waves at high Froude numbers. *Physics of Fluids*, 17, 36602.

Colombini, M. & Stocchino, A. (2008) Finite-amplitude river dunes. *Journal of Fluid Mechanics*, 611, 283–306.

Colombini, M. & Stocchino, A. (2012) Three-dimensional river bed forms. *Journal of Fluid Mechanics*, 695, 63–80.

Deigaard, R. (2006) Breaking antidunes: cyclic behavior due to hysteresis. *Journal of Hydraulic Engineering*, 132(6), 620–623.

Dhont, B. & Ancey, C. (2018) Are bedload transport pulses in gravel-bed rivers created by bar migration or sediment waves? *Geophysical Research Letters*, 45, 5501–5508.

Di Cristo, C., Iervolino, M. & Vacca, A. (2006) Linear stability analysis of a 1-D model with dynamical description of bed-load transport. *Journal of Hydraulic Research*, 44(4), 480–487.

Dressler, R.F. (1978) New nonlinear shallow-flow equations with curvature. *Journal of Hydraulic Research*, 16, 205–222.

Dressler, R.F. & Yevjevich, V. (1984) Hydraulic-resistance terms modified for the Dressler curved-flow equations. *Journal of Hydraulic Research*, 22(3), 145–156.

Einstein, H.A. (1942) Formulas for the transportation of bed load. *Transactions of the American Society of Civil Engineers*, 107, 561–597.

Engelund, F. (1970) Instability of erodible beds. *Journal of Fluid Mechanics*, 42, 225–244.

Froude, M.J., Alexander, J., Barclay, J. & Cole, P. (2017) Interpreting flash flood palaeoflow parameters from antidunes and gravel lenses: An example from Montserrat, West Indies. *Sedimentology*, 64(7), 1817–1845.

Furbish, D.J., Haff, P.K., Roseberry, J.C. & Schmeeckle, M.W. (2012) A probabilistic description of the bed load sediment flux: 1. Theory. *Journal of Geophysical Research*, 117, F03031.

Furbish, D.J. & Roering, J.J. (2013) Sediment disentrainment and the concept of local versus nonlocal transport on hillslopes. *Journal of Geophysical Research*, 118, 937–952.

Gilbert, G.K. & Murphy, E.C. (1914) The transportation of débris by running water. Technical report, U.S. Geological Survey Professional Paper, 86. Washington: US Government Printing Office, pp. 1–263.

Gomez, B., Naff, R.L. & Hubbell, D.W. (1989) Temporal variations in bedload transport rates associated with the migration of bedforms. *Earth Surface Processes and Landforms*, 14, 135–156.

Grant, G.E. (1994) Hydraulics and sediment transport dynamics controlling step-pool formation in high gradient streams: a flume experiment. *Dynamics and geomorphology of mountain rivers*. Berlin: Springer, pp. 241–250.

Greco, M., Iervolino, M. & Vacca, A. (2018) Analysis of bedform instability with 1-D two-phase morphodynamical models. *Advances in Water Resources*, 120, 50–64.

Guala, M., Singh, A., BadHeartBull, N. & Foufoula-Georgiou, E. (2014) Spectral description of migrating bed forms and sediment transport. *Journal of Geophysical Research: Earth Surface*, 119, 123–137.

Guo, J. (2015) Sidewall and non-uniformity corrections for flume experiments. *Journal of Hydraulic Research*, 53(2), 218–229.

Guy, H.P., Simons, D.B. & Richardson, E.V. (1966) Summary of alluvial channel data from flume experiments, 1956-61. *U.S. Geological Survey Professional Paper*, Vol. 462-I. Washington, US: US Government Printing Office, pp.1–196.

Hayashi, T. (1970) Formation of dunes and antidunes in open channels. *Journal of the Hydraulics Division*, 96, 357–366.

Heyman, J., Bohorquez, P. & Ancey, C. (2016) Entrainment, motion, and deposition of coarse particles transported by water over a sloping mobile bed. *Journal of Geophysical Research: Earth Surface*, 121, 1931–1952.

Huang, L.-H. & Chiang, Y.-L. (2001) The formation of dunes, antidunes, and rapidly damping waves in alluvial channels. *International Journal for Numerical and Analytical Methods in Geomechanics*, 25(7), 675–690.

Inoue, T., Watanabe, Y., Iwasaki, T. & Otsuka, J. (2020) Three-dimensional antidunes coexisting with alternate bars. *Earth Surface Processes and Landforms*, 45(12), 2897–2911.

Johnson, J.W. (1942) The importance of side-wall correction in bed-load investigation. *Civil Engineering*, 12(6), 329–331.

Kennedy, J.F. (1961) Stationary waves and antidunes in alluvial channels. Ph.D. Thesis, California Institute of Technology.

Kennedy, J.F. (1963) The mechanics of dunes and antidunes in erodible-bed channels. *Journal of Fluid mechanics*, 16(4), 521–544.

Kennedy, J.F. (1969) The formation of sediment ripples, dunes, and antidunes. *Annual Review of Fluid Mechanics*, 1, 147–168.

Kubo, Y. & Yokokawa, M. (2001) Theoretical study on breaking of waves on antidunes. In: Peakall, J., McCaffrey, W. & Kneller, B. (Eds.) *Particulate Gravity Currents*. IAS Special Publication no. 31. Oxford: Blackwell Science, pp. 65–70.

Mettra, F. (2014) Morphodynamic mechanisms in steep channels: from local processes to large-scale evolution. Ph.D. Thesis, École Polytechnique Fédérale de Lausanne.

Núñez-González, F. & Martín-Vide, J.P. (2011) Analysis of antidune migration direction. *Journal of Geophysical Research: Earth Surface*, 116(F2), 1–16.

Nikora, V. (1984) The structure of turbulent flow and statistical characterisation of dune-covered river beds (with examples of field studies in rivers Turunchuk, Rioni, and Tsheniscali). Ph.D. Thesis. Leningrad/St Petersburg: State Hydrological Institute.

Palucis, M.C., Ulizio, T.P., Fuller, B. & Lamb, M.P. (2018) Flow resistance, sediment transport, and bedform development in a steep gravel-bedded river flume. *Geomorphology*, 320, 111–126.

Parker, G. (1975) Sediment inertia as cause of river antidunes. *Journal of Hydraulic Division*, 101, 211–221.

Recking, A., Bacchi, V., Naaim, M. & Frey, P. (2009) Antidunes on steep slopes. *Journal of Geophysical Research*, 114, F04025.

Recking, A., Frey, P., Paquier, A., Belleudy, P. & Champagne, J.Y. (2008) Feedback between bed load transport and flow resistance in gravel and cobble bed rivers. *Water Resources Research*, 44, W05412.

Reynolds, A.J. (1965) Waves on the erodible bed of an open channel. *Journal of Fluid Mechanics*, 22(1), 113–133.

Shaw, J. & Kellerhals, R. (1977) Paleohydraulic interpretation of antidune bedforms with applications to antidunes in gravel. *Journal of Sedimentary Research*, 47(1), 257–266.

Simons, D.B., Richardson, E.V. & Nordin, C.F. (1965) Bedload equation for ripples and dunes. U.S. Geological Survey Professional Paper, Vol. 462-H. Washington: US Government Printing Office, pp. 1–9.

Singh, A., Fienberg, K., Jerolmack, D.J., Marr, J. & Foufoula-Georgiou, E. (2009) Experimental evidence for statistical scaling and intermittency in sediment transport rates. *Journal of Geophysical Research*, 114, 2007JF000963.

Slootman, A. & Cartigny, M.J.B. (2020) Cyclic steps: review and aggradation-based classification. *Earth-Science Reviews*, 201, 102949.

Tucker, G.E. & Bradley, D.N. (2010) Trouble with diffusion: reassessing hillslope erosion laws with a particle-based model. *Journal of Geophysical Research*, 115, F00A10.

Vesipa, R., Camporeale, C. & Ridolfi, L. (2012) A shallow-water theory of river bedforms in supercritical conditions. *Physics of Fluids*, 24, 94104.

Vesipa, R., Camporeale, C., Ridolfi, L. & Chomaz, J.-M. (2014) On the convective-absolute nature of river bedform instabilities. *Physics of Fluids*, 26, 124104.

Whittaker, J.G. & Jaeggi, M. (1982) Origin of step-pool systems in mountain streams. *Journal of the Hydraulics Division*, 108(6), 758–773.

SUPPORTING INFORMATION

Additional supporting information may be found online in the Supporting Information section at the end of this article.

How to cite this article: Pascal I, Ancey C, Bohorquez P. The variability of antidune morphodynamics on steep slopes. *Earth Surf. Process. Landforms*. 2021;46:1750–1765. https://doi.org/10.1002/esp.5110